NIR Silicon Photodetector Enhancement Using Photonic Crystal Cavity Resonators

by

Ebrahim Dakhil Al Johani

Submitted to the Department of Physics
in partial fulfillment of the requirements for the degree of

Bachelor of Science in Physics

at the

MASSACHUSETTS INSTITUTE OF TECHNOLOGY

June 2019

Author .....
Department of Physics
May 10th, 2019

Signature redacted

Certified by.... .....
Rajeev J. Ram
Professor of Electrical Engineering
Thesis Supervisor

Signature redacted

Certified by..... .....
Marin Soljačić
Professor of Physics
Thesis Supervisor

Signature redacted

Accepted by... .....
Nergis Mavalvala
Associate Department Head, Department of Physics

NIR Silicon Photodetector Enhancement Using Photonic Crystal Cavity Resonators

by

Ebrahim Dakhil Al Johani

Submitted to the Department of Physics
on May 10th, 2019, in partial fulfillment of the
requirements for the degree of
Bachelor of Science in Physics

Abstract

The growing demand for efficient infrared sensors for light ranging, thermal-cameras, and soon, free-space optical communications has yet to be answered. In this study, we use polycrystalline silicon in conjunction with a photonic crystal cavity (PhCC) to enhance light absorption for efficient sensing. We present a cost-effective alternative to the current III-V detectors. By adding a 2D-PhC resonator layer, surface-illuminated light can be confined within a 10 micron region with great intensity, leading to a higher effective path-length and improved detector responsivity. More than 1000 variants of this detector are designed and implemented in a 65nm CMOS process. Using a nearest neighbor method, we find the optimized designs. We validate experimental findings by simulating mode behavior of the PhCC structures using FDTD models. In addition, a numerical study on cavity parameter optimization for achieving high Q-factors and extinction ratios specifically for surface-illumination is presented. We report polysilicon PhCC-enhanced sensors with Q-factors of 6500 resulting in responsivities at 1300nm up to 0.13mA/W —a 25x improvement over non-resonant surface-illuminated Silicon detectors.

Thesis Supervisor: Rajeev J. Ram
Title: Professor of Electrical Engineering

Thesis Supervisor: Marin Soljačić
Title: Professor of Physics

Acknowledgments

I would like to thank Professor Rajeev J. Ram for the unique opportunity to delve into the world of device physics and for his guidance throughout my undergraduate journey. I would also like to thank Dr. Amir Atabaki for his work that went into this thesis and his technical guidance and mentorship. Finally, I would like to thank all my friends and family for their continued support and wishes.

Contents

List of Figures

List of Tables

Chapter 1

Introduction

1.1 Background

The goal of the research presented is to enable the advancement of near-infrared (NIR) technologies. The increase in demand on efficient sensors for light ranging, thermal-cameras, and soon, free-space optical communications is resulting in a gap between the commercial needs and the state-of-the-art. Basic research that aims to examine material and physical limitations is essential for addressing this demand.

Silicon is becoming the most widely used material in fiber-based communication for its integrability with most electronics [15]. Leveraging the complementary metal-oxide-semiconductor (CMOS) for silicon caused many of these advancements. This thesis aims to build on the current theory and technology and leverage it into the free-space environment. Using the NIR range to send and receive information between objects in a short-ranged environment, while maintaining eye-level safe emissions, is one of the biggest challenges for current free-space NIR applications.

The indirect bandgap of crystalline silicon poses some optical limitations. An indirect transition constrains the crystal to undergo a momentum exchange every time a photon is absorbed or emitted, which reduces light absorption dramatically. In addition, NIR wavelength photons have lower energy than the bandgap of silicon and cause even lower levels of generation. However, there are a few phenomena that could be harnessed to enable sub-bandgap absorption; these include surface-state-

assisted, virtual-state-assisted, as well as phonon-assisted absorption which allow for more than one low energy mechanism to add their energies and overcome the gap [5].

The aforementioned effects result in an absorption depth of crystalline silicon around the order of 10^4 cm at 1300 nm and orders of magnitude higher at longer wavelengths [14]. This sets a research challenge which is currently being tackled from different directions.

1.2 Previous Works in Free Space NIR Enhancement of Si

An early method to enhance low-absorbing silicon is to expose it to high levels of deuteron and neutron radiation. The damages radiation caused to the crystal creates mid-bandgap states that ultimately lower the weak-absorption effects [5]. A different method utilizes the Schottky diode effect where a metal layer is placed near the semiconductor junction. The electrons generated near the metal surface carry kinetic energy, which allows it to overcome the energy gap [2]. This method, however, requires applying a high external reverse voltage to provide electrons with a high enough energy. Moreover, a common method found in the literature uses light confining structures to increase the effective path-length of light in the material. Resonance-enhanced devices add a Fabry-Perot cavity, creating an enhancement factor given by Q/V where Q is the quality factor of the resonator and V is the mode volume [6, 27].

Casalino's 2010 review paper describes the various mechanisms sub-bandgap absorption can occur. Out of the four mechanisms, the internal photoelectric effect (IPE) and two photon absorption (TPA) are the most utilized in engineering detector junctions for sub bandgap photons. The paper then proceeds to provide examples of architectures that apply these absorption mechanisms. The highest responsivity devices reported were the Schottky and resonator designs with 2.3-13.3 mA/W and 0.25mA/W, respectively [31, 13, 8].

Unfortunately, the methods highlighted in Casalino's review paper and briefly in

the beginning of this section have a common issue. The purpose of using silicon is to utilize the platform's well-established technology. Yet previous enhancement techniques modify the devices beyond what is permitted by current CMOS standards [5]. Hence, a CMOS-compatible enhancement mechanism called photonic crystal (PhC) microcavities is proposed as an alternative method. Photonic crystals have proven to be efficient structures to control light. By engineering a periodic dielectric structure, it is possible to create in-plane light-confining structures that are compatible with the silicon CMOS environment [17, 4]. Experimental work in waveguide-based and thermophotovoltaic devices have demonstrated an increase in photocurrent generation through the use of PhC microcavities [25, 23]. In addition, considerable advancement in waveguide TPA detectors has been demonstrated in CMOS for interconnect application. [19, 21]. However, more work has yet to be shown for surface-illuminated TPA detector structures in more CMOS-compatible packaging. To our knowledge, outside of on-chip waveguide structures, PhCs have not been used as a sub-bandgap enhancement mechanism in CMOS.

Surface-illuminated structures have been demonstrated in III-Vs, and as far as . In quantum cascade detectors, a PhC is used as a coupling mechanism to direct incident light into a transverse resonance. It is also shown to increase its photocurrent absorption at resonance ($\lambda = 9\mu m$) and lowers the noise power [22]. Such advances have also been demonstrated in quantum-well infrared detectors. Normal incident light on a PhC layer on the surface of detector created sharp peaks in photocurrent generation at mid IR wavelengths ($\lambda = 7.6\mu m$) [18].

1.3 Introduction to Photonic Crystal Cavities

As alluded to in the previous section, there are a number of ways to enhance light absorption and one of the main methods is by implementing a light confining structure. Examples of structures include Fabry-Perot resonators and rough surfaces (or more elegant, pyramid structures). However, most (if not all) designs found in the literature cannot be efficiently integrated into the CMOS environment. The search

for a small footprint detector, compatible with CMOS, lead to a type of in-plane resonating structures termed photonic crystal cavities.

Any structure with a periodic dielectric function is termed a photonic crystal. 1D, 2D, and 3D photonic crystals correspond to periodicities in one, two, and three dimensions [16]. Simply from this setup we arrive to interesting light propagation properties. Assuming separable spatial and temporal dependencies of the electric and magnetic field propagating in the medium, we can rewrite Maxwell's equations (neglecting electric and current source terms) as an eigenvalue equation,

$$\nabla \times \left(\frac{1}{\epsilon(\mathbf{r})}\nabla \times \hat{\mathbf{H}}(\mathbf{r})\right) = \left(\frac{\omega}{c}\right)^2 \hat{\mathbf{H}}(\mathbf{r}). \tag{1.1}$$

The eigenvalue in this case is $(\frac{\omega}{c})^2$, a real quantity. Hence, this complicated operator is Hermitian and analogous to the Hamiltonian operator in quantum mechanics. This equation holds all the information needed to describe light propagation in a varying dielectric medium.

In the case where $\epsilon(r)$ is periodic, solutions to this eigenvalue problem become more manageable. Under periodic conditions, solutions must take the same periodicity as its environment. This is known as Bloch's Theorem. Applying it to the equation above,

$$\mathbf{H}_k(\mathbf{r}) = e^{i\mathbf{k}\cdot\mathbf{r}}\mathbf{u}_k(\mathbf{r}) \tag{1.2}$$

where $\mathbf{u}_k(\mathbf{r})$ is periodic with the same period of the dielectric function, i.e. $\mathbf{u}_k(\mathbf{r}) = \mathbf{u}_k(\mathbf{r}+\mathbf{R})$. For some dielectric function, a mode can have any arbitrary shape within a unit cell.

1.3.1 Photonic Band Gap and Defect States

The previous solution's periodicity is the only condition needed to show one of the most defining features of a photonic crystal: its bandgap. Due to the symmetry of the structure, the nodes of the propagating wave must be at the center of either the low-index or the high index regions. This is illustrated in Figure 1-1. Given these two modes, most of the energy of the wave then is localized either in the high index

region, corresponding to a node in the center of the low-index region or most of the energy will be in the low index region, corresponding to a node in the center of the high-index region. The two modes of this structure have the same periodicity, but one is in a higher index region than the other. The only way to resolve two waves with equal wavevectors but propagate in different mediums is if they carry different energies. Hence, this can be visualized by a jump in frequency between the two modes. This jump is illustrated in Figure 1-1.

Modes that propagate in the high-index region are said to be propagating in the Dielectric Band, whereas modes that propagate in the low-index region are said to be propagating in the Air Band. In between is a gap where no modes exist. The gap is called a photonic bandgap.

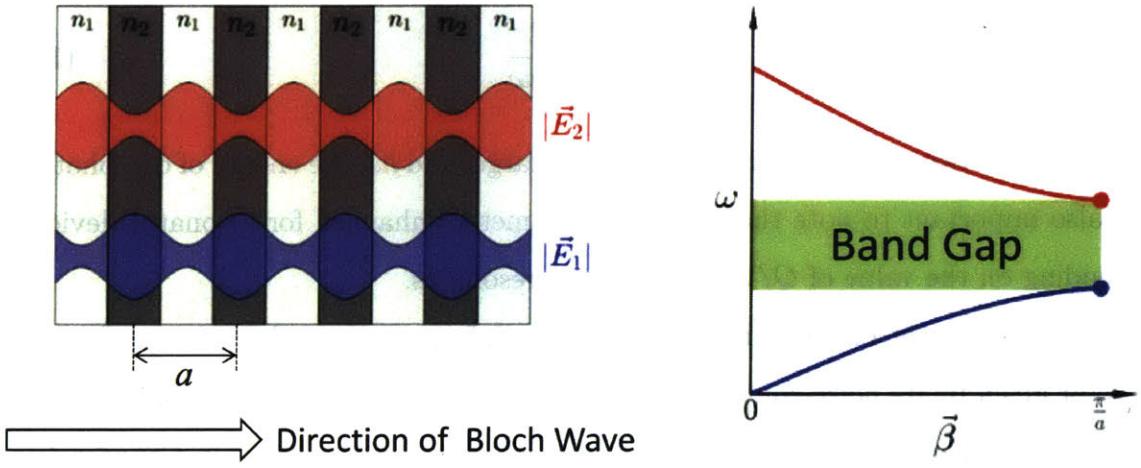

Figure 1-1: (a) Two modes propagating in a periodic dielectric medium (b) The wavelength separation of the two modes

Furthermore, introducing a defect to this perfectly periodic structure, such as a change in the index of one unit cell or the spacing between two unit cell boundaries, has interesting consequences. Due to this symmetry breaking, the area near this change there will allow for modes to propagate within the bandgap. There will be a defect state that exists while completely surrounded by forbidden regions. Depending on the nature of the crystal and defect, the mode can be strongly localized in one, two, or three dimensions in a very selective wavelength.

This simple idea has been the basis of many important highly localized, highly selective, devices such as phase-modulators, VCSELs, and cavity electrodynamics [24, 9, 28]. In this thesis, we extend the application of photonic crystal cavities to the area of free-space NIR detectors.

1.4 Evaluation Metrics

The first photodetector figure of merit generally used is the responsivity. At a given wavelength, the responsivity of a detector encodes information on its conversion efficiency, which is normally stated as the detector's quantum efficiency. The quantum efficiency, or ηQE, is all the internal mechanisms and generation that give rise to a photon-electron conversion rate. It is found by the expression

$$\eta_{QE} = \frac{R}{q/\hbar\omega} \tag{1.3}$$

where R is the responsivity, q the elementary charge, and $\hbar\omega$ the energy of one photon. It is also important to note that R is the parameter enhanced for resonator devices. Depending on the value of Q/V, the detector resonates.

The dark current on the other hand encodes information on the noise profile of a detector given by its noise-equivalent power or NEP. More on the noise and dynamic range figures of merit will be discussed towards the end of the thesis in Chapter 4.

Another key metric that is helpful in characterizing the device but is the bandwidth of device. The bandwidth is a measure of how fast the detector responds and differentiates between two successive signals. This metric is extremely important in high-speed applications such as optical modulators and light communication; however, since this application is targeted for free-space detection, its importance drops since the bottleneck will more likely include external factors such as propagation distance and medium.

To summarize, there are two directly measurable figures-of-merit to extract and

Reference	Type Device	Material	Responsivity (mA/W)	Dark current (pA)	Wavelength (nm)	NEP ($pW/H^{1/2}$)
Casalino et al. (2012)[7]	F–P microcavity enhanced	Silicon, 100μm depth	0.063	3.5×10^9 (-0.1V)	1550	**5.3e5**
Amirmazlaghani et al. (2013)[3]	–	Graphene-Silicon Schottky junction	9.9 (-16V)	2.4×10^6 (-16V)	1550	**88.6**
Desiatov et al. (2015)[11]	Silicon Pyramids (apex ~$50\mu m^2$)	Al–Silicon Schottky junction	12 (-100mV)	8×10^4 (-100mV)	1300	**13.3**
Alloatti et al. (2016)[2]	Lateral PN, 45nm CMOS (12SOI)	SiGe, 10μm x 10μm	0.032	10 (-2V)	1080	**56**
Casalino et al. (2017)[8]	F–P cavity enhanced	Graphene–Silicon Schottky junction	20 (-10V)	0.15×10^9 (-10V)	1550	**350**
Tanzid et al. (2018)[26]	Plasmonic and Free Carrier of highly doped Si	Au-Pd grating 0.9x0.5μm	10^3 (-275mV)	3.5 (-275mV)	1375	**10**

Figure 1-2: An overview of the literature of NIR silicon based surface-illuminated detectors, and their various enhancement mechanisms. Key metrics in the devices are shown. NEP estimated based on shot-noise statistics of dark current and responsivity if not reported.

optimize for, the responsivity and dark current. These two metrics tell us how efficient a device is under certain illuminations and what is the minimum detected power, respectively. In addition, due to the nature of our device, we can compare the same characteristics on and off-resonance, Q-factors, and coupling factors. Figure 1-2 presents an overview of the literature of Si-based NIR detectors.

1.5 Thesis Overview

This work approaches the problem described in Section 1.1 in mainly two ways. Chapter 2 addresses the integration problem by presentings empirical results of surface-illuminated device fabricated in CMOS-compatible process. The layout and process is described in Section 2.1. Then Section 2.2 refers to the main the IV curve as the first element of characterization in a PD. Although binary, the measurement lead to a class of devices with favorable electrical characteristics for PD operation. Two setpus were used to measure the behavior of the devices in different methods of illumination: a free-space setup, 2.3, and a lensed-fiber setup, 2.4. Section 2.3.1 and 2.4.1 follow with a spectral analysis of the resonance enhancement due to the PhCC. Different

figures-of-merit were determined (e.g. responsivity and dynamic range) based on the setup.

In Chapter 3 a discusses the structure optimization problem using FDTD simulations. The first beacon used to guide the design is described in Section 3.3 where the photonic bandgap is calculated. A discussion on the contributing Q factors follows in Section 3.4 as well as results of the simulation for the cavity parameters used for the optimization.

Lastly, Chapter 4 reflects on the empirical and numerical results in a discussion on noise (Section 4.1) and numerical simulations (Section 4.2), and concludes with an overview and future work.

Chapter 2

Experimental Characterization of PhCC Detectors

PhC cavities are structures characterized by their enhancement factor, Q/V. Like any resonator, this factor fully describes the cavity losses independent from the characteristic scale of the resonator. Higher enhancement factor lead to larger free-spectral-ranges paired with high selectivity (small resonator bandwidth); this is a desirable effect regardless of the application as it enables increased spectral resolution over a larger range. We are able to estimate the Q/V value by drawing from key features of measured data and simulations. For example, a comparison between on and off resonance photocurrent leads to estimating the enhancement in the detector's sensitivity. The higher the enhancement factor, or extinction, the more sensitive the device is to incident light of that wavelength. Since PhC cavities are known to be efficient light confining structures at extremely narrow linewidths, we expect the detectors to be narrowband as well.

Photodetectors are primarily characterized by their current responses with varying voltage, wavelength and input power. The first section discusses the general layout and fabrication process then each following section discusses a different characterization measurement.

2.1 Layout and Fabrication

The photonic devices' layout consists of 1088 devices that are designed in an industry standard design tool, Cadence Virtuoso, by a research scientist in our lab, Amir Atabaki. The designs are then implemented in a 65nm CMOS process and fabricated on 300mm wafers at the Center for Nanoscale Science & Engineering (CNSE).

There are three main reasons for a test space this large. The first reason is that cavities are extremely sensitive to their length scales and there is some uncertainty in the dimensional control for the layers used to define the PhC. Hence, sweeping a cavity size will lead to higher confidence in the designs and length scales (i.e. neighboring devices will perform similarly unless there is in error); this can also be seen from Appendix A.2. Second, having a diverse test space is useful to quantify the fit between a particular design with photodetector. This is particularly important since both optical modeling and carrier transport simulations are computationally taxing. And lastly, as the major driving force, the overhead cost of a small design scales marginally with increasing chip real estate. Adding more designs is more favorable economically.

Each device is approximately $12\mu m$ wide (diameter) and 220nm thick. A diagram of a sample design showing the different parameters is shown in Figure 2-1.

This base structure is designed to balance between confinement and coupling. For example, a structure that is able to confine light well will likely have low coupling with incident light; whereas a structure that can easily couple to incident light will be a poor resonator. Therefore, there is some optimum design between the two extremes at critical coupling. The metric used in the literature to describe this tradeoff along with the resonator overall is the Q/V enhancement factor. To maximize the detector performance a critically coupled resonator with high Q-factors and smaller modal volumes is desirable.

Each device consists of a unique set of six parameters that together determine the bandgap, coupling efficiency, and center resonance wavelength. The parameters are shown in Table 2.1 with their range of values. Most of the parameters are self-evident. For example, a is the radii of the periodic holes, and r_d is the resizing of

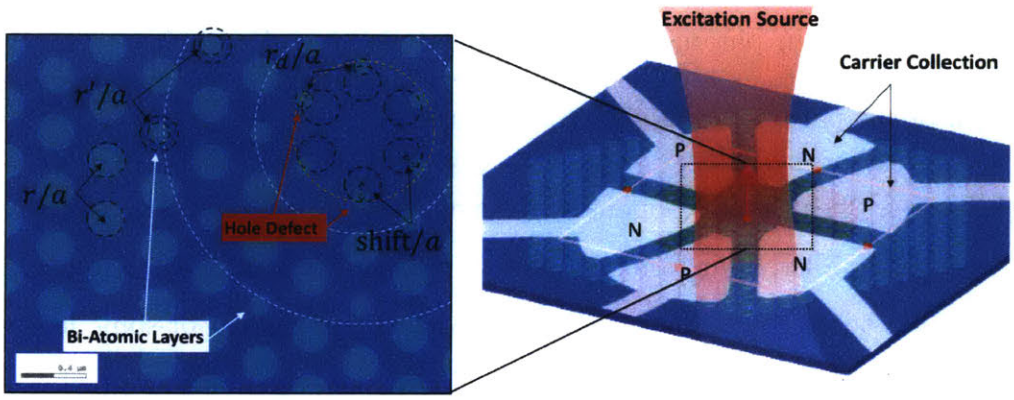

Figure 2-1: Diagram of device structure under illumination. On the detector side, the P and N doped regions form a spokes-on-a-wheel shape to collect minority carriers more efficiently as there is less length needed to diffuse through. On the PhC side, the field intensity is maximum when centered within the intrinsic region where the defect lies. Exact dimensions and scale layout of the device and chip can be found in Appendix A.1

radii near the defect. However, the second radius and defect layers require further elaboration. Since the structures are limited in lateral distance, there is a need to increase the in-plane coupling with incident light. The idea here is to introduce a perturbation that is symmetric in the xy-plane such that the effective defect will have a stronger z-component coupling. Having this image in mind, a selection of holes is shrunk symmetrically in layers surrounding the defect. The final defect structure takes a bi-atomic shape. The degree of shrinkage (r'/a) and number of layers affected (Defect Layers) is varied.

2.2 Characteristic I-V

One of the most insightful characteristics of a detector is its response to an applied voltage, both forward and in the reverse direction. The forward direction shows

Lattice Constant (a)	0.37 - 0.40μm	r_d/a	0.1 - 0.2
r/a	0.17 - 0.35	Defect Shift/a	0.1 - 0.25
r'/a	0.17 - 0.35	# Defect Layers	1-3

Table 2.1: The six design parameters for the photonic crystal and their respective values. Values are swept to create 1088 different variants of detector design. A visual representation of the parameters is shown in Figure 2-1

whether there is a "healthy" exponential relation between current and voltage as would be expected in a PIN junction. A different relation such as linear or quadratic would suggest that there is an abnormally high tunneling of current or some leakage. Such a response implies that the detector junction is somewhat ill-designed or, in worst cases, damaged.

Moreover, in reverse bias, we expect for a well-behaving device to have a reasonably high breakdown voltage and low current dependence on reverse-bias (as the diode equation suggests reverse-bias current is given by optical generation and leakage), and also the operation noise level and dynamic range.

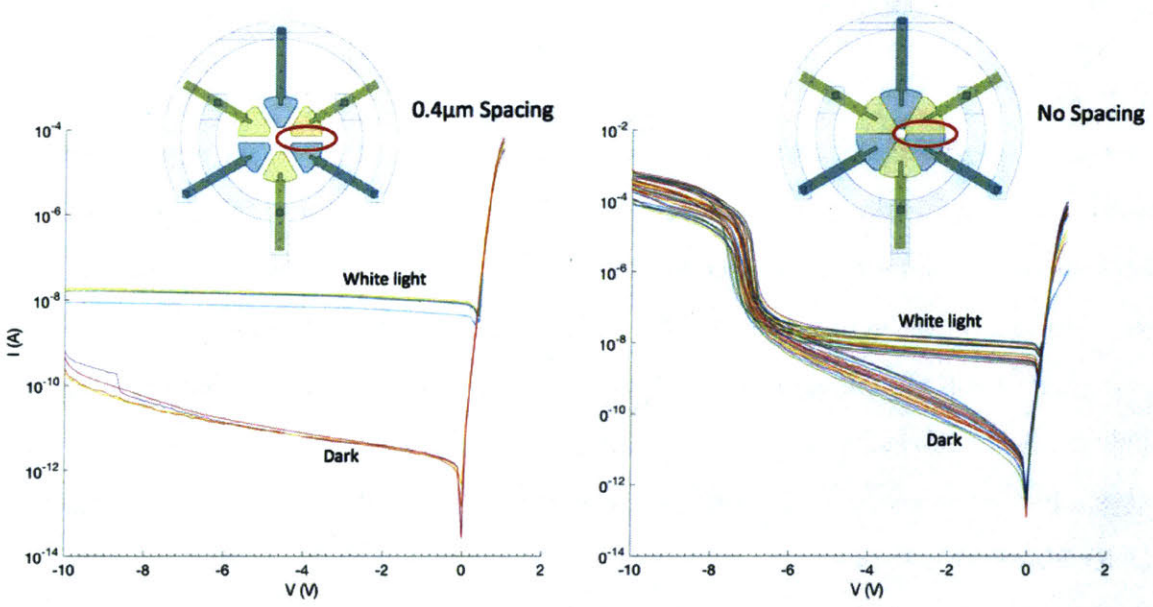

Figure 2-2: IV of two types of devices: with 0.4μm PN spacing (a) 0.0μm PN spacing (b) where both are measured under direct white-light illumination and dark conditions. A diagram of the corresponding device junctions is shown above its I-V

Figure 2-2 shows the I-V of various measured devices. Out of the tested devices the I-V characteristic is overwhelmingly determined by a single junction parameter.

The shape of the device junction is circular with P and N regions combining in the middle making a shape that resembles spokes on a wheel. The spacing between where the different spokes meet is varied and chosen to be either $0.4\mu m$ or $0.0\mu m$. When the spacing is $0.4\mu m$, the I-V curve has a more traditionally, well-behaved shape: a high breakdown voltage ($\approx -16V$) and low current dependence in reverse bias. However, when the spacing is removed, the favorable diode-like characteristics diminish, a large tunneling current, an increase in noise, and a premature breakdown is observed.

Even though they are the minority out of the 1088 devices, we focus the analysis on the $0.4\mu m$ PN spacing devices as they present the more favorable diode characteristic curve and dynamic range. We report a dark current on this type of device of $3.9pA$ at $2V$ reverse bias.

2.3 The Free-Space Setup

Some of the applications this thesis is aimed at considering the Fraunhofer approximation of planar electromagnetic waves. Free-space communication for example, looks at planar waves and their interactions with matter.

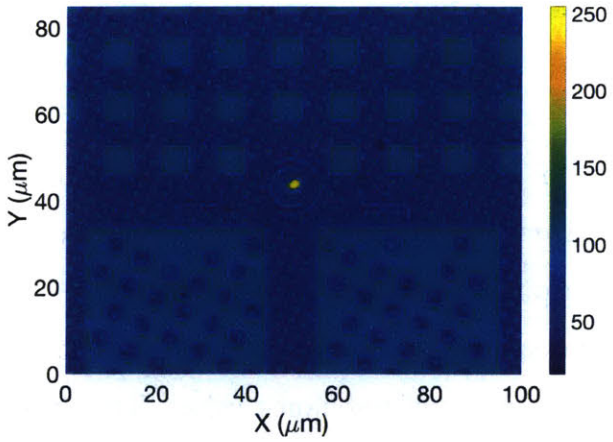

Figure 2-3: An intensity bitmap (0-256) collected from the InGaAs camera sensor depicting the laser-detector alignment method. The axes are scaled to show distance (centered at an arbitrary location). A fine-coarse nob on the laser xy translation cage is used to maximize for the photocurrent.

In this setup, we use a 20x NIR Mitutoyo objective (WD = 20mm) to focus a

free-space beam of 1300nm laser onto the PhC chip. The beam is then aligned using an InGaAs camera sensor (Xenics's Xeva 1.7) on the surface of the on-chip detector. The image we see from this setup is shown in Figure 2-3

2.3.1 Spectral Response

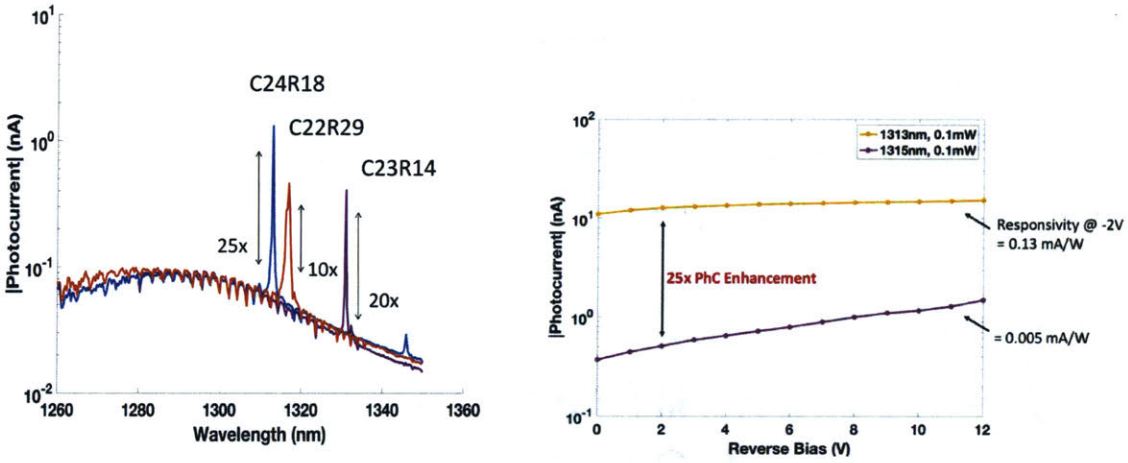

Figure 2-4: (a) Spectral responses of devices C24R18, C22R29, and C23R14 and their respective extinction ratios. The Q factors of the devices in order are 6565, 1317, and 6655. (b) I-V curve of C24R18 on and off-resonance in reverse bias. The devices are named based on their location on the chip (where C corresponds to the device's column, and R to its row)

Table 2.2 presents the cavity parameters of the three devices with the highest Q-factors. A reverse bias plot of the highest device is shown in Figure 2-4.

The resonance mode of the cavity is largely sensitive to changes in wavelength, down to the order of $0.1nm$ (FWHM). The spectra measured of the three devices shows the common background where the photonic crystal is insensitive to the color of light. However, a slight change into the resonance results in a 25, 20, and 10 times increase in photocurrent than its off-resonance value. The optical power of light is kept constant while sweeping the frequency; due to this fact, the responsivity of the devices is also enhancement by the same factors.

As a point of comparison, a 220nm thick slab of crystalline silicon has an absorption depth of $12.5 \times 10^4\ 1/cm$ at $1.33\mu m$ [14]. For such an absorption and slab thickness the quantum efficiency (assuming no reflection on surface) is $\eta_{QE} = 1.76 \times 10^{-9}$

and a responsivity of $R = 1.89 \times 10^{-6}\ mA/W$.

Device	R_1/a	R_2/a	R_d/a	Shift/a	Layers
C23R14	0.31	0.31	0.2	0.1	3
C22R29	0.297	0.33	0.2	0.1	3
C24R18	0.33	0.33	0.2	0.1	3

Table 2.2: PhCC parameters of the three highest performing devices (shown in Figure 2-4)

2.3.2 Supermodal Splitting

Resonance splits (referred to as supermode splitting) as shown in Figure 2-5 have been observed in PhCC designs. Splits occur when a vital parameter to the resonance is adjusted (through the defect or its environment), while keeping the surrounding lattice untouched [3]. Such a modification creates a superposition of modes between the pre-existing mode before the modification and the nearest mode after the modification. It is called a supermode due to the presence of two or more interacting modes in the cavity. The most commonly used alteration in the literature to the defect are shrinking and shift away from center.

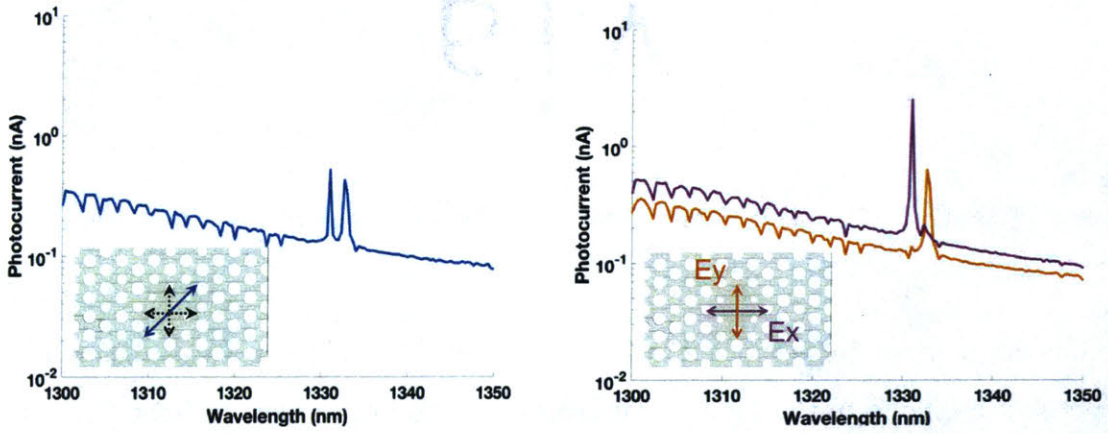

Figure 2-5: The illumination of mixed polarization light (a) and two perpendicularly polarized lights. (b) Resonance shifts based on the 90° symmetry-break in the hexagonal structure and additional alterations in the structure of the defect.

This discussion suggests that there is still room for additional optimization of the PhCC structure. A solution towards this could be to find 'opposite' modifications

such that the net effect on resonance wavelength is zero. This level of understanding of photonic crystal cavities would lead to an enhanced efficiency and better coupling. Thus, some numerical analysis is needed to further solve the structure.

2.4 The Lensed-Fiber Setup

To understand the device operation under direct fiber excitation we use a $2.5\mu m$ beam-waist lensed fiber in our setup in place of the focusing objective. The fiber along with a responsivity measurement is shown Figure 2-6. The working distance of the fiber is $10 - 15\mu m$

2.4.1 Spectral Response

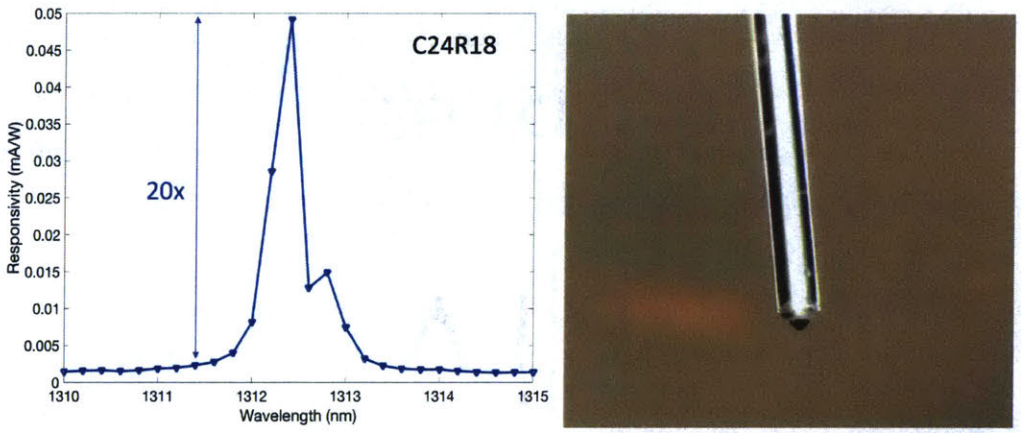

Figure 2-6: (a) plot of the responsivity against wavelength. The input optical power is set to 0.9mW with a set reverse bias of 2V. (b) an image of the tip of the lensed fiber.

The discrepancy between the Far Field ($0.13mW/A$) and Near Field ($0.05mW/A$) responsivities is due to the limited polarization control of the lensed fiber setup. As seen in Figure 2-6, there is some energy in the split-off mode. The mode splitting in addition to the lack of polarization control poses serious concerns: a lower extinction ratio (20x instead of the 25x seen in far field) and much lower Qs. There are two methods that can be used to resolve this discrepancy. One way is optimize the design such that there is no resonance split as discussed in 2.3.2. Chapter 3 will go over

some of the theory of defect design and optimization. The second, less favorable alternative, is to operate the device under a polarization controlled system.

2.4.2 Spot Size & Linear Dynamic Range

Before characterizing the spot size, it is essential to determine the linear operating range of the detector. Generally, in a photodetector, there exists a range where the incident power is linear with photocurrent. This region, between the noise level and current saturation, is called the linear dynamic range or LDR of the detector. A plot of this range is shown in Figure 2-7.

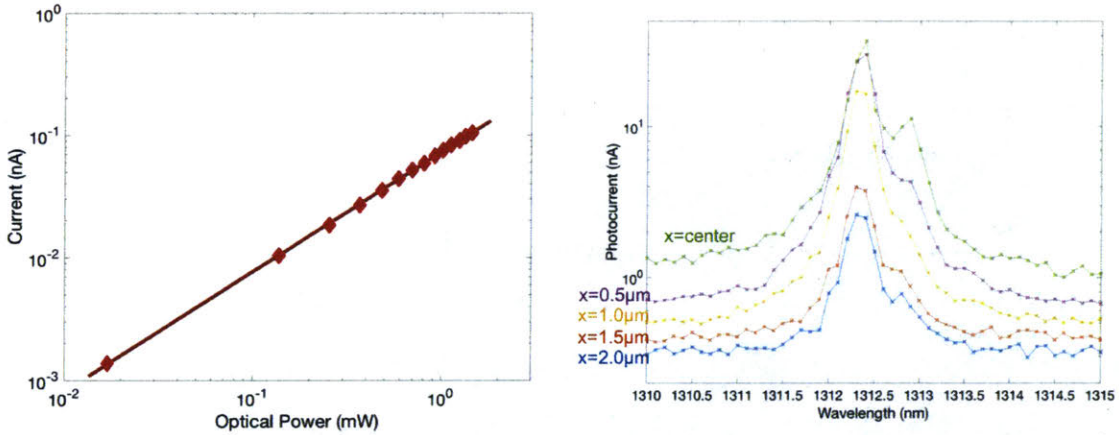

Figure 2-7: (a) A plot of the LDR (40dB) of the photodetector at a CW and -2V operating point.(b) spectral response at various distances away from the center of the cavity. The device C23R14 is used.

As expected, to be seen in a high-quality silicon microelectronic process, the LDR of the fabricated devices is high with a reasonably low noise floor making the device more sensitive even at low input powers/responsivities. Moving forward, it can be assumed that all experimental data is taken in the LDR of detectors.

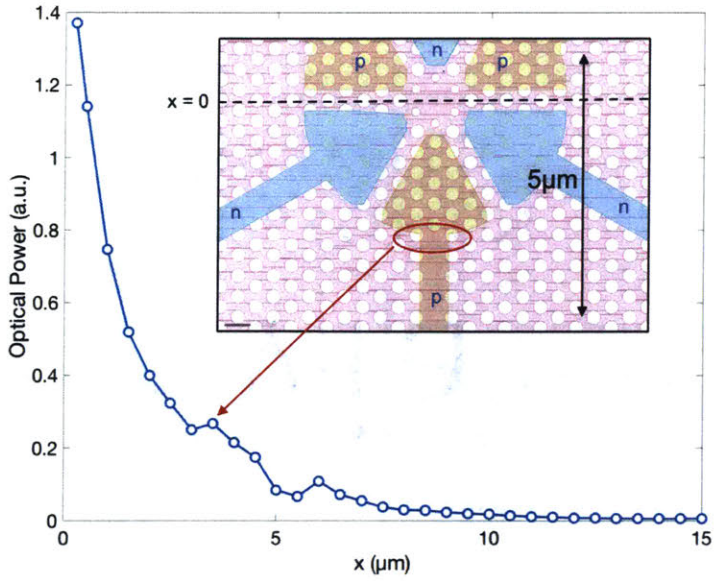

Figure 2-8: (left) A measurement of current plotted against fiber position, x (where $x = 0$ is the center of the defect). A discontinuity in the current response is seen at the same distance as the discontinuity in crystal structure.

Furthermore, a scan of the power against spot location is needed to understand the incident wave profile. Figure 2-8 shows a plot for estimating the spot-size of the beam. Using a lensed fiber, and assuming a Gaussian profile, a general approximation of the beam waist can be determined. The plot shows a very sharp drop in intensity after approximately $3\mu m$ which agrees with an approximate analytical calculation of the beam waist of $3.2\mu m$ calculated from the knife-edge measurement formula (provided in Appendix A.3).

Chapter 3

PhCC Theory & Simulation

3.1 Overview

In this chapter, Section 3.2 begins by defining some of the key elements in numerical modeling and its application to this work. The following sections go over the results of the simulations, and various setups used to deduce the coupling efficiency, Q-factor, and other key metrics.

3.2 Notes on Software and Resonator Design

In conjunction with experimental verification, it is useful to investigate the theoretical limit of devices performance. Fabricating and testing can easily become intractable, especially with large overhead costs. Therefore, researchers have developed numerical tools to model light-matter interaction which avoids risks and opens more avenues of exploration. Some of the tools used are a Finite-Difference Time-Domain (FDTD) analysis and Field-Element Method (FEM) along with many others.

In this work, we use an industry-standard field simulation tool, Lumerical Solutions, and the MIT Electromagnetic Equation Propagation (MEEP) library to model and test the PhC cavities we have [20]. Both Lumerical and MEEP use FDTD. A 3D simulation of the PhCC slab mode made in Lumerical is shown in Figure 3-1.

MEEP is used to visualize the cavity mode and calculate the transmission spec-

trum of the cavity modes. We implement the cavities structure in a Python script (Appendix B.1) and use the same designs from fabricated array. The goal is to model and verify the experimental results as well as predict trends. There will be however limitations to this method since the real devices do not exist in vacuum but are surrounded by various layers of dielectric masks that increase the complexity of the structure. In the MEEP simulations, we build a copy of the PhCC without the additional layers. For the MEEP calculations in 3.3 and 3.5 a 2D photonic crystals is implemented with $n_{polySi} = 3.5$ and $n_{SO_2} = 1.5$.

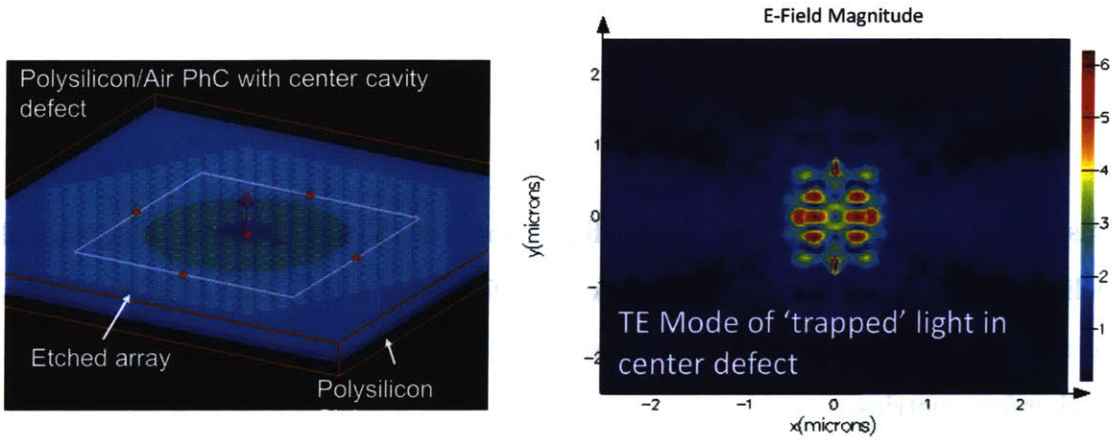

Figure 3-1: Simulated PhC cavity in Lumerical. (a) Photonic crystal cavity structure made to visualize modes and field intensity. Materials used polysilicon and air with indices 3.5 and 1 respectively. (b) Color bar showing the magnitude of E/E_{Norm}. C23R14 PhCC structure is used.

3.3 Band Structure

Characterizing a PhC begins by first engineering the bandgap. Since the range of frequencies is chosen based on the fabricated devices. We hope to find bandgaps that cover a portion of the NIR range (namely $1.1 - 1.6\mu m$). The type of photonic crystal we've chosen are thin slab 2D-PhC with triangular lattice arrangement. To solve for the band structure we use the MIT Photonic Bandgap (MPB) package provided by MEEP. The geometry is defined with a lattice constant and radii as shown in Figure 3-2. The primary Brillouin zone $\vec{k}$ vectors (Γ, K, M) are defined as described in the

figure as well as the number of bands to calculate. A quick simulation shows that a full bandgap is present between frequencies $0.48-0.79$ (c/a) for a lattice constant and radius of $0.4\mu m$ and $0.33a$ respectively which is indeed spanning the desired range.

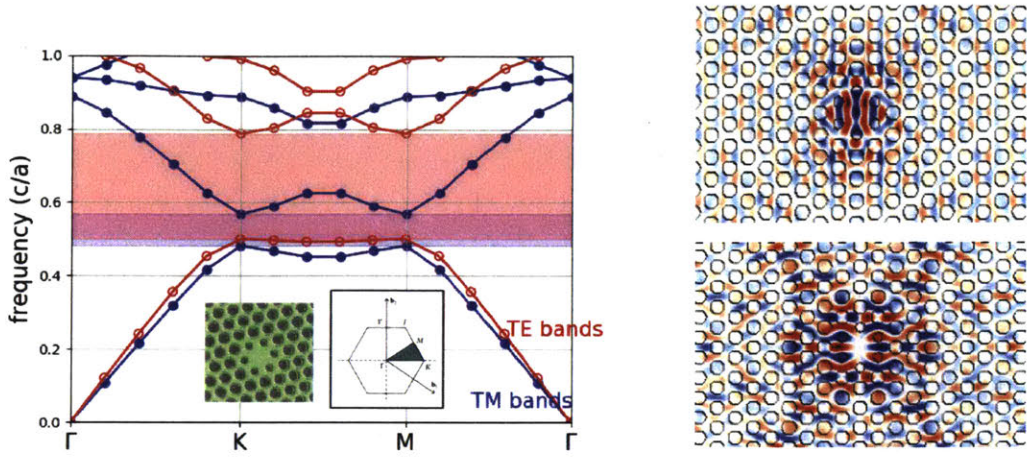

Figure 3-2: (a) Calculated band structure (4 bands) in MPB for both TE and TM modes. The shaded regions show the the photonic bandgap for (red) TE and (blue) TM modes. The geometry is defined to be an infinite triangular PhC with $a = 0.4\mu m$ and $r = 0.33a$. (b-c) Finite-Difference simulation used on C23R14 photonic crystal (with $n_{polySi} = 3.5$ and $n_{SO_2} = 1.5$) to determine resonance strength and coupling. Source is modeled as a Gaussian current point-source centered at 1330nm with σ=300nm. (b) Hy polarized (c) Hx polarized

Removing a single unit cell from the lattice introduces modes within the bandgap. Light of the frequency is trapped as if in a perfect mirror. Light of that frequency is able to resonate with Q-factors of 1.5-3k. Diagrams of the resonant $\hat{\mathbf{H}}_y$ and $\hat{\mathbf{H}}_z$ modes are also shown in Figure 3-2.

A few questions remain unanswered, however. For example, it is still unclear how do different cavity parameters effect the resonance wavelength. A possible approach to answer this question is to calculate the transmission spectrum of the structures for different defect types.

3.4 Cavity Modes & Coupling Efficiency

Given the finite thickness of the 2D PhC slab in Figure 2-1, light is confined in both in-plane via the PhC and out-of-plane via the dielectric slab. The given ge-

ometry has several effects on the loss and coupling efficiency of the cavity. Analyzing a 3-dimensions can quickly become complicated and computationally intractable, however, there are two ideas shown in previous work that take advantage of the pronounced symmetry of this structure as well as some knowledge in the eigenmodes [30, 29, 11]. The relation between the total Q and its in-plane and out-of-plane components can be drawn from energy conservation:

$$\frac{1}{Q} = \frac{1}{Q_{\perp}} + \frac{1}{Q_{\parallel}}. \tag{3.1}$$

The equation suggests that by making a larger lattice, $Q_{\parallel}$ can be arbitrarily high. The limiting factor in photonic crystal slabs' confinements becomes $Q_{\perp}$.

The second idea can be seen from the perspective of waveguide theory. A mode propagating in a slab with thickness d (220nm in our experimental case) has an effective index lower than the material index. The broadening due to this effect reduces the overlap between the photonic crystal and the mode. The same conclusion can be reached from the perspective of PhC theory; it can be thought of as the low index contrast pushes the bandgap to lower frequencies. The next two topics address the PhCC coupling problem through optimizing for the discussed structures.

3.5 Transmission Spectra

Furthermore, it is important to understand the characteristics of the cavity (or defect) when different alterations are applied. Figure 3-3 and 3-4 show two different experiments highlighting the effects of defect and lattice alterations on the Q.

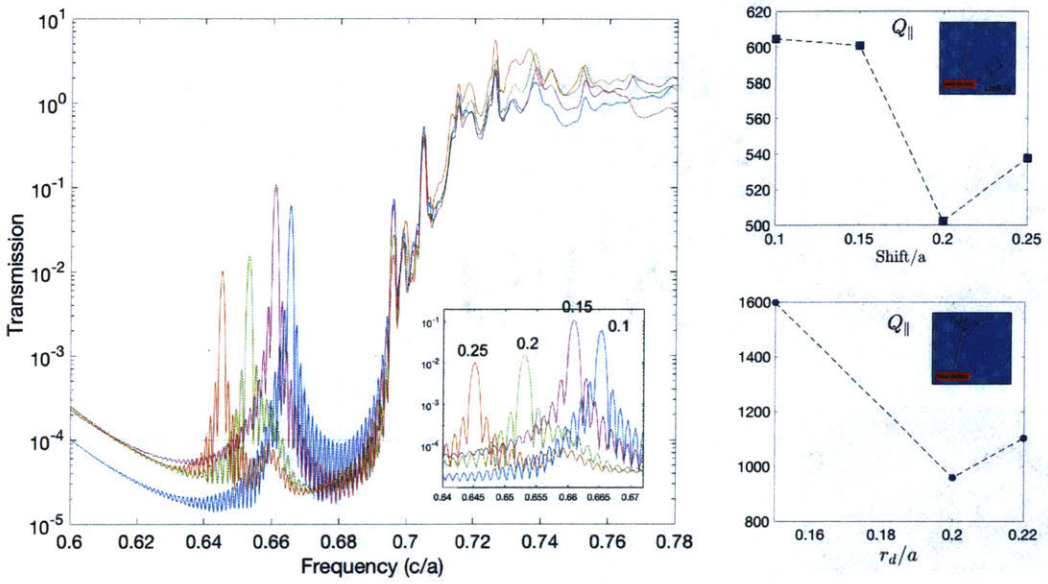

Figure 3-3: (a) A 2D MEEP transmission calculation of four PhCCs with different defect shifts based on the C23R14 parameters. A closeup of the cavity resonance is shown on the bottom right corner with the corresponding shift values. (b) Quality factor as function of normalized shift parameter ($r_d/a = 0.2$) (c) Quality factor as a function of the normalized defect resizing with $shift/a = 0$, and all other parameters held constant.

In both experiments, we place a gaussian dipole source in the center of the cavity centered at the resonance frequency. Next, we place a flux region calculator surrounding the slab which measures the in-plane Poynting vector flux exiting the region. The calculation of $Q_\perp$ provides us with the sufficient lattice size to maximize the total Q. Normalizing the output of the flux calculation to the initial intensity of dipole outputs the transmission at of the slab per frequency.

In Figure 3-3 we compare the transmission loss between an altered and unaltered cavity; more specifically, we apply the shrink parameter to the unit cells surrounding the lattice.

In Figure 3-4, on the other hand, we show the effect of increasing the size on

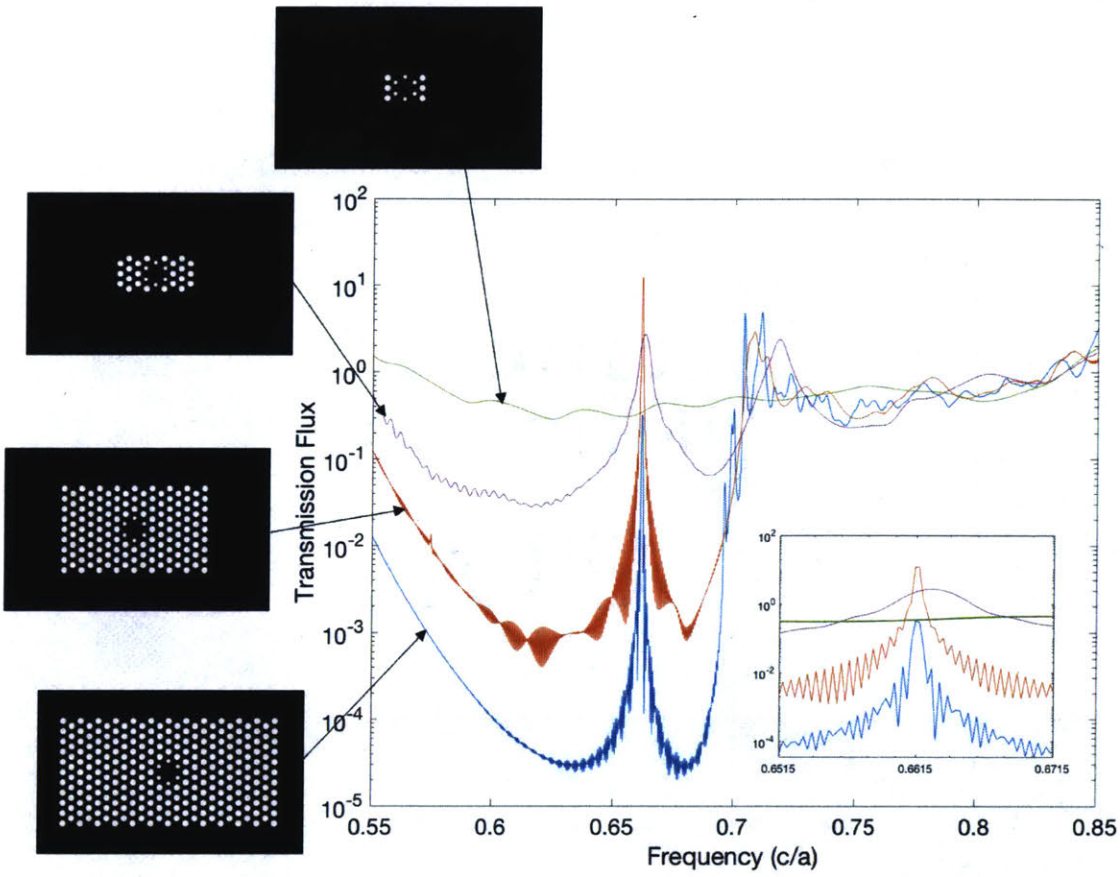

Figure 3-4: In-plane (2D) transmission of four different PhC slab sizes with the same identical cavity (C23R14) implemented in MEEP. a-d) Triangular PhCC lattices with sizes 5×5, 9×9, 20×20 (Q = 1102), and 30×30 (Q = 1655).

$Q_{\parallel}$ (and thereby the total Q). Since a finite size crystal is not a perfectly periodic environment, the bandgap is not well defined. However, with a sufficiently large crystals $Q_{\parallel}$ can be arbitrarily high. From the plot shown, as we expected, increasing the size reduces loss and increases the Q-factor.

An interesting by-product is that the enhancement factor slightly goes down from Figure 3-4c to 3-4d. The slight drop of the extinction makes sense since a perfect resonator would not allow any light to escape, so the extinction goes down even though there is higher internal confinement (i.e. $Q_{int} > Q_{ex}$).

Chapter 4

Discussion

After both empirical and numerical analysis of the photonic crystal cavity detectors, this section focuses on the implication and interpretation of the results. In this Section 4.1, we also discuss one of the most important metrics for a detector, its detectivity, and how it compares with other enhancement mechanisms. Section 4.2, notes the extent and limitations of the numerical model developed.

4.1 Noise

In summary of the past sections, the analysis provided in this chapter shows that it is possible to determine the total incident power, estimate the spot size, and finally, calculate the dynamic range given values of the responsivity and dark count rate. On resonance, the responsivity of the enhanced detector is $0.1mA/W$. The dark current, on the other hand, can be determined using the shot noise relation.

With more than one noise source in a detector, it can easily get difficult to measure. In the literature, it is common practice to estimate the most dominant type of noise as the first order approximation to noise analysis. [12] We can reduce the problem by assuming a uniform illumination source and a linear efficiency. It follows that the noise expression reduces to primarily current generated during the absence of a signal either through electrical noise or background light. This type of noise is usually referred to as the dark current Shot Noise and is regarded as a Poissonian random

process since the arrival events are temporally sparse and uncorrelated. The variance of current produced through this white noise process is given in the expression,

$$\langle i_s^2 \rangle = 2qI_d\Delta f, \tag{4.1}$$

where I_d is the dark current, q is the charge of the electron, and Δf is the noise spectrum range.

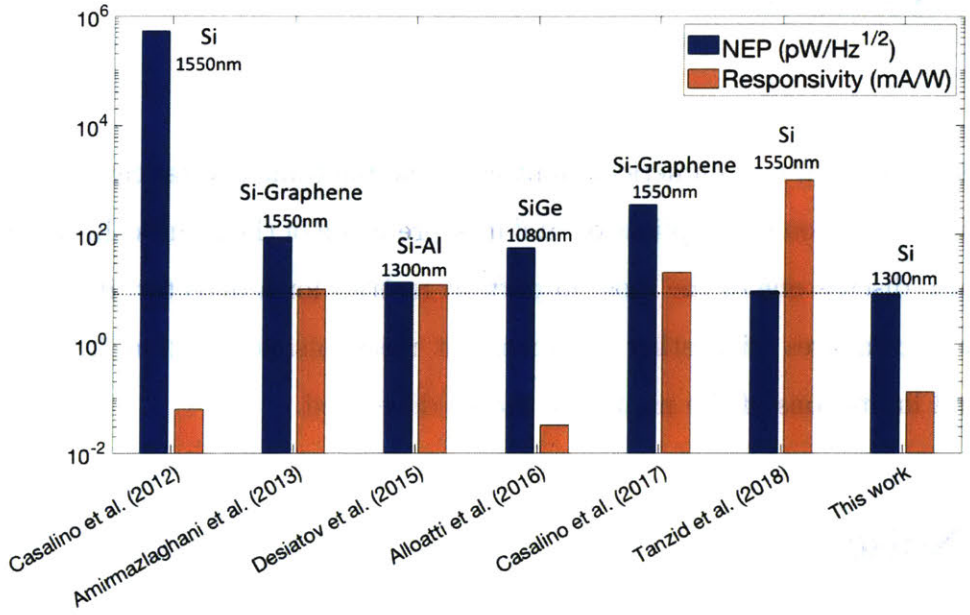

Figure 4-1: A comparison between different infrared Silicon detector in the literature showing their estimated NEP, based on the dark current and responsivities at given biases.

With a dark current of $3.5pA$ and a given responsivity as well as a poissonian model of shot noise, it's possible to estimate a value for the noise-equivalent power (NEP). NEP is a notable figure-of-merit which encodes information on the sensitivity of the device. It is usually expressed in $W/\sqrt{Hz}$ and is given by the expression,

$$NEP = \frac{1}{R}\sqrt{\frac{\langle i_s^2 \rangle}{\Delta f}} = \frac{\sqrt{2qI_d}}{R}, \tag{4.2}$$

where R is the responsivity. The intuitive explanation of NEP is that it describes how much power is needed to overcome the internal noise of the device and generate

an "on" signal. The lower the value, the less power is needed to reliably identify a presence of a signal. Hence, 1/NEP is naturally referred to as the detectivity, D, of the device. Using the values and expressions above the PhCC device has a NEP of approximately $8.2pW/\sqrt{Hz}$ assuming a flat spectral range of Δf .

Figure 4-1 presents various devices in the literature that use different materials and enhancement mechanisms as discussed in previous sections. As shown, even with a responsivity of only $0.13mA/W$ the devices presented in this work, with their high dynamic range, provide the lowest NEP, and therefore, the highest detectivity.

4.2 Numerical Agreement

This work reports a resonance enhancement empirically and numerically developed PhCC slab constructed using polycrystalline silicon. In both cases, we note a strong confinement within relatively narrow bands ($Q \sim 10^3$). Using a lattice constant of $a = 0.4\mu m$ and rod radii of around $r/a = 0.31 - 0.33$, and height of 220nm we have demonstrated that photonic bandgaps act as a highly selective filters for telecom, and more broadly NIR wavelengths. By tuning the parameters of the defect cavity it is possible to fine-adjust the peak resonance. Figure 4-2 applies the numerical model developed to the three highest performing measured devices.

The figure reveals the agreement between the model and experimental trend by solely adjusting the lattice and defect parameters shown in Table 2.1. The predictive power of the model lies in revealing the effect of a change i.e whether this change will increase or decrease the resonance wavelength and the quality factors, even for complicated changes (such as the alternating bi-atomic effect). This model, however, does not predict the exact location of the peaks; as discussed in Section 3.2 this requires knowledge of the surrounding environment of the fabricated PhC slab (e.g. surrounding structure, surrounding indices, doping density, temperature) which is process dependent, and less generally applicable. For this reason, we see a different peak wavelength when directly comparing experimental (1313, 1317, and 1331nm) and numerical (1503, 1520, and 1543nm) results as shown in Figure 4-2.

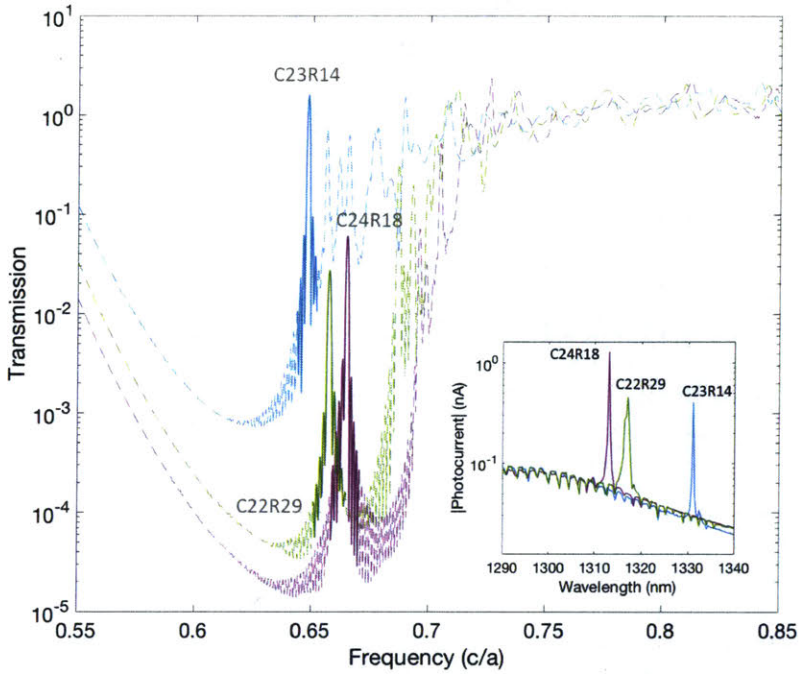

Figure 4-2: A trend comparison between experimental and simulation results for the best preforming devices in Table 2.2. The speed of light, c, is set to unity, thus the frequency is related to the wavelength in through $f = \frac{1}{\lambda}$.

4.3 Conclusion

Optimized PhCC structures have been presented with Q-factors up-to 6500 and high extinction peaks due to Q/V of the order $10^{16}\ cm^{-3}$. The purpose of using PhCC structures is to provide the missing link for surfaces-illumined detectors by efficiently coupling incident beams into transverse layers giving a CMOS-compatible design. The same devices have been numerically visualized and verified using FDTD. Design matrices such as photonic crystal size and defect parameter allocation has been optimized for critical coupling with surface-illuminated light. Additional optimization of the PhCC can also be an area of future work. For example, introducing slab thickness and dielectric constant variation in the model can further guide future design iterations, specifically for CMOS environments.

With a dark current of 3.5pA we can estimate the shot noise in a Poissonian process, that gives an NEP of 8.2 $(\frac{pW}{\sqrt{Hz}})$, the lowest value in comparison with de-

tectors in Figure 4-1. Although responsivities are below commercial III-V detectors (0.9W/A), the high signal-to-noise ratio at zero-bias and integration into microelectronic processes opens countless possibilities for the future of PhCC detectors. A notable possibility is an array of packaged PhCC detectors with a cascaded high-gain Trans-Impedance Amplifier (TIA) to create a multidirectional, narrowband, NIR sensor die.

Finally, this work demonstrates that through using a resonance layer it is possible to enhance the sub-bandgap responsivity of polycrystalline silicon to an order of $0.1mA/W$.

Bibliography

[1] L. Alloatti and R. J. Ram. Infrared vertically-illuminated photodiode for chip alignment feedback. *AIP Advances*, 6(8), 2016.

[2] M. Amirmazlaghani, F. Raissi, O. Habibpour, J. Vukusic, and J. Stake. Graphene-Si schottky IR detector. *IEEE Journal of Quantum Electronics*, 49(7):589–594, 2013.

[3] K. Atlasov, K. F. Karlsson, A. Rudra, B. Dwir, and E. Kapon. Observation of wavelength- And loss-splitting of supermodes in coupled photonic-crystal microcavities. *2008 Conference on Quantum Electronics and Laser Science Conference on Lasers and Electro-Optics, CLEO/QELS*, pages 3–4, 2008.

[4] J. Bravo-Abad, E. P. Ippen, and M. Soljačić. Ultrafast photodetection in an all-silicon chip enabled by two-photon absorption. *Applied Physics Letters*, 94(24):2007–2010, 2009.

[5] M. Casalino, G. Coppola, M. Iodice, I. Rendina, and L. Sirleto. Near-infrared sub-bandgap all-silicon photodetectors: State of the art and perspectives. *Sensors*, 10(12):10571–10600, 2010.

[6] M. Casalino, G. Coppola, M. Iodice, I. Rendina, and L. Sirleto. Critically coupled silicon Fabry-Perot photodetectors based on the internal photoemission effect at 1550 nm. *Opt Express*, 20(11):12599–12609, 2012.

[7] M. Casalino, U. Sassi, I. Goykhman, A. Eiden, E. Lidorikis, S. Milana, D. De Fazio, F. Tomarchio, M. Iodice, G. Coppola, and A. C. Ferrari. Vertically Illuminated, Resonant Cavity Enhanced, Graphene-Silicon Schottky Photodetectors. *ACS Nano*, 11(11):10955–10963, 2017.

[8] H. Chen, X. Luo, and A. W. Poon. Cavity-enhanced photocurrent generation by 1.55 wavelengths linear absorption in a p-i-n diode embedded silicon microring resonator. *Applied physics letters*, 95(17):171111, 2009.

[9] K. D. Choquette, D. F. Siriani, A. M. Kasten, M. P. Tan, D. Joshua, P. O. Leisher, J. J. R. Jr, and A. J. Danner. Single Mode Photonic Crystal Vertical Cavity Surface Emitting Lasers. *Advances in Optical Technologies*, 2012, 2012.

[10] B. Desiatov, I. L. Y. A. Goykhman, N. Mazurski, J. O. Shappir, J. B. Khurgin, and U. Levy. Plasmonic enhanced silicon pyramids for internal photoemission Schottky detectors in the near-infrared regime. *Optica*, 2(4):335–338, 2015.

[11] D. Englund, D. Englund, I. Fushman, and J. Vuckovic. General recipe for designing photonic crystal cavities. *Optics express*, 13(16):5961—-5975, 2005.

[12] Y. Fang, A. Armin, P. Meredith, and J. Huang. Accurate characterization of next-generation thin-film photodetectors. *Nature Photonics*, 13(January):1–4, 2019.

[13] I. Goykhman, B. Desiatov, J. Khurgin, J. Shappir, and U. Levy. Locally Oxidized Silicon Surface-Plasmon Schottky Detector for Telecom Regime. *Nano Letters*, 11(6):2219–2224, 2011.

[14] M. A. Green. Self-consistent optical parameters of intrinsic silicon at 300 K including temperature coefficients. *Solar Energy Materials and Solar Cells*, 92(11):1305–1310, 2008.

[15] B. Jalali and S. Fathpour. Silicon Photonics. *Journal of Lightwave Technology*, 24(12):4600–4615, 2006.

[16] J. D. Joannopoulos, S. G. Johnson, J. N. Winn, and R. D. Meade. *Photonic Crystals: Molding the Flow of Light.* Princeton University Press, 2007.

[17] J. D. Joannopoulos, P. R. Villeneuve, and S. Fan. Photonic crystals: putting a new twist on light. *Nature*, 386(6621):143, 1997.

[18] S. Kalchmair, R. Gansch, S. I. Ahn, A. M. Andrews, H. Detz, T. Zederbauer, E. Mujagić, P. Reininger, G. Lasser, W. Schrenk, and G. Strasser. Detectivity enhancement in quantum well infrared photodetectors utilizing a photonic crystal slab resonator. *Optics Express*, 20(5):5622, 2012.

[19] K. K. Mehta, J. S. Orcutt, O. Tehar-Zahav, Z. Sternberg, R. Bafrali, R. Meade, and R. J. Ram. High-Q CMOS-integrated photonic crystal microcavity devices. *Scientific Reports*, 4:1–6, 2014.

[20] A. F. Oskooi, D. Roundy, M. Ibanescu, P. Bermel, J. D. Joannopoulos, and S. G. Johnson. Meep: A flexible free-software package for electromagnetic simulations by the FDTD method. *Computer Physics Communications*, 181(3):687–702, 2010.

[21] C. V. Poulton, X. Zeng, M. T. Wade, J. M. Shainline, J. S. Orcutt, and M. A. Popović. Photonic crystal microcavities in a microelectronics 45-nm SOI CMOS technology. *IEEE Photonics Technology Letters*, 27(6):665–668, 2015.

[22] P. Reininger, B. Schwarz, A. Harrer, T. Zederbauer, H. Detz, A. M. Andrews, R. Gansch, W. Schrenk, and G. Strasser. Photonic crystal slab quantum cascade detector. *Applied Physics Letters*, 103(24):1–5, 2013.

[23] C. Shemeya and T. E. Vandervelde. Comparison of photonic-crystal-enhanced thermophotovoltaic devices with and without a resonant cavity. *Journal of Electronic Materials*, 41(5):928–934, 2012.

[24] M. Soljacic, S. G. Johnson, S. Fan, M. Ibanescu, E. Ippen, and J. D. Joannopoulos. Photonic-crystal slow-light enhancement of nonlinear phase sensitivity. *Journal of the Optical Society of America*, 19(9):2052–2059, 2002.

[25] T. Tanabe, H. Sumikura, H. Taniyama, A. Shinya, and M. Notomi. All-silicon sub-Gb/s telecom detector with low dark current and high quantum efficiency on chip. *Applied Physics Letters*, 96(10):2–5, 2010.

[26] M. Tanzid, A. Ahmadivand, R. Zhang, B. Cerjan, A. Sobhani, S. Yazdi, P. Nordlander, and N. J. Halas. Combining Plasmonic Hot Carrier Generation with Free Carrier Absorption for High-Performance Near-Infrared Silicon-Based Photodetection. *ACS Photonics*, 5(9):3472–3477, 2018.

[27] K. J. Vahala. Optical microcavities. *Nature*, 2003(August):352, 2003.

[28] J. Vučković, M. Lončar, H. Mabuchi, and A. Scherer. Design of photonic crystal microcavities for cavity QED. *Physical Review E - Statistical Physics, Plasmas, Fluids, and Related Interdisciplinary Topics*, 65(1):1–11, 2002.

[29] J. Vuckovic, M. Loncar, H. Mabuchi, and A. Scherer. Optimization of the Q Factor in Photonic. *IEEE Journal of Quantum Electronics*, 38(7):850–856, 2002.

[30] T. Yoshie, J. Vu{\v{c}}kovi{\'c}, A. Scherer, H. Chen, and D. Deppe. High quality two-dimensional photonic crystal slab cavities. *Applied Physics Letters*, 79(26):4289—-4291, 2001.

[31] S. Zhu, G. Q. Lo, and D. L. Kwong. Low-cost and high-speed SOI waveguide-based silicide Schottky-barrier MSM photodetectors for broadband optical communications. *IEEE Photonics Technology Letters*, 20(16):1396–1398, 2008.

Appendix A

Empirical Analysis

A.1 Chip Layout & Design

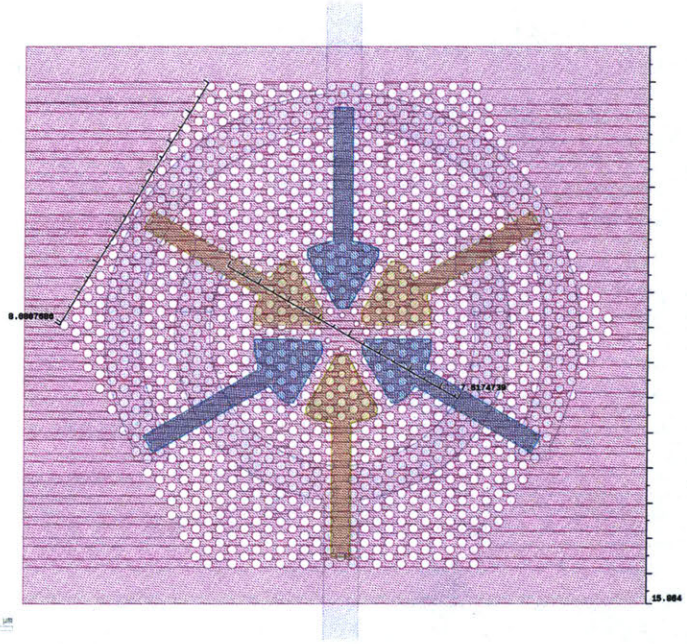

Figure A-1: The layout of a typical device with annotated dimensions and scale. The pink (square) layer is the photonic crystal made of 220nm think foundry-grade (low defect density) intrinsic poly-silicon. Cyan and brown (rail) regions are p-doped and n-doped poly-silicon respectively to create the photodiode junction. The shape was chosen to maximize for the minority-carrier diffusion length into a nearby intrinsic region while maintain low breakdown voltages and noise current. The doped regions are connected to the Al circular regions through three vias each. The metal regions ultimately terminate at the landing pads used to probe the device. The pitch between the pads is $20\mu m$ hence a $50\mu m$ pitch GS probes is used.

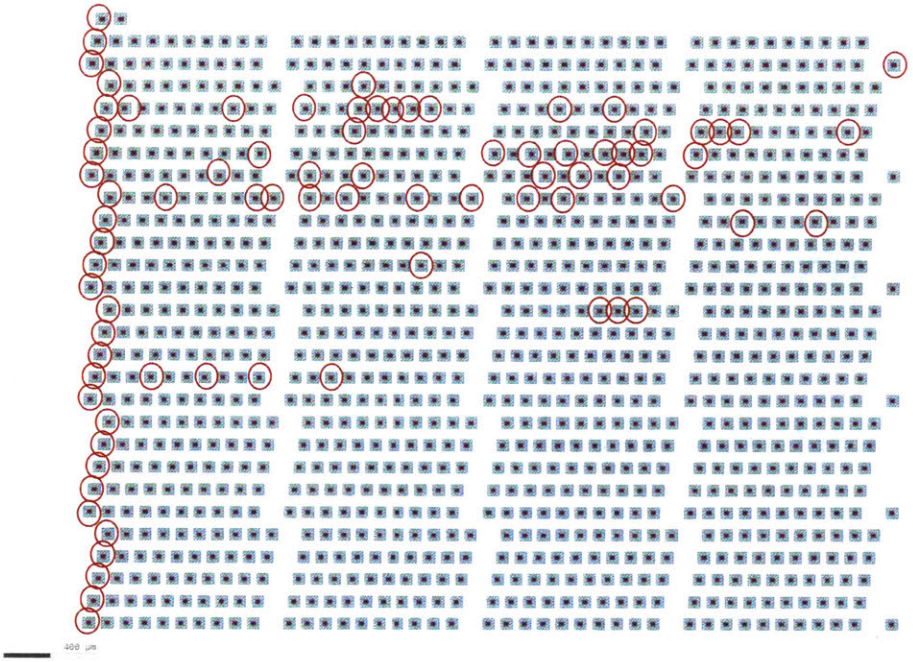

Figure A-2: Layout of parameter search space of 1088 PhCC devices used to narrow down highest performing devices. Highlighted in red (circles) are experimentally tested and characterized devices (+150 devices). Most devices exhibited limited-to-no spectral responses. The presented devices were chosen (excluded) based on the parameter-space nearest-neighbor performance and those which show positive (negative) correlation with the presence strong resonance. Among the excluded devices are all those with lattice constants of 0.37 and $0.43\mu m$, and those with $0.0\mu m$ PN spacing (+750 devices)

A.2 Fabrication Dimensional Tolerances

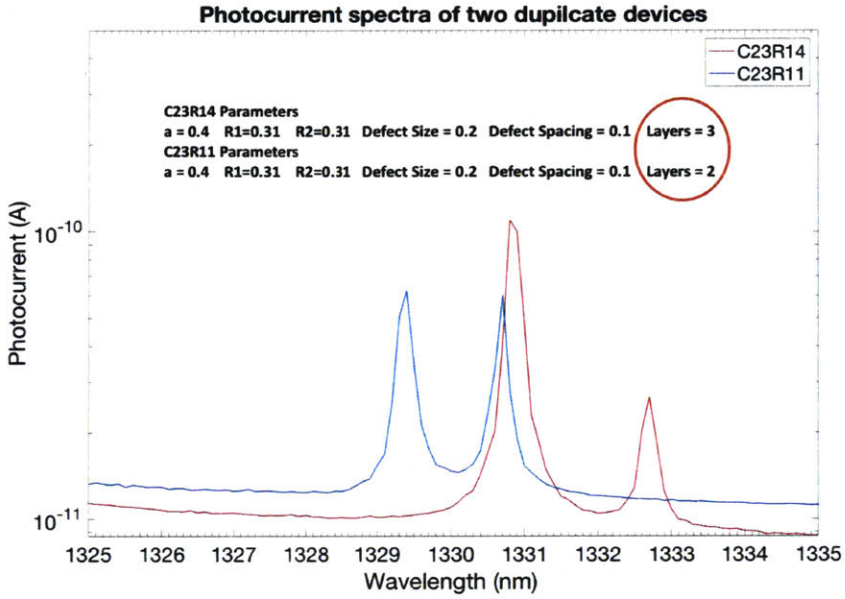

Figure A-3: Two spectra corresponding to devices C23R11 and C23R14. The two devices have identical parameters except for the bi-atomic layer parameter (circled in red).

$R1$ and $R2$ in Figure A-3 are identical in both devices. Hence, the readjustment of the layers surrounding the hole does not have an overall effect on the structure. Even though initially there was no intention of fabricating duplicates, their existence turns to be an insightful piece of information. As discussed in 2.1, slight inaccuracies in the fabrication of the devices lead to variations in the peak (supermode) resonances. Each curve shows the resonance split but the curves are slightly shifted. This can result from any rough edges or dielectric variation near the defect.

A.3 Knife-Edge Measurement Formula

Knife-edge measurements are used to estimate the beam waist of a gaussian beam by using a precise, sharp edged tool (such as a knife). By sweeping the location of the knife between the beam and some power sensor, the sensor side will see,

$$P(x) = P_0 + \frac{P_{max}}{2}\left(1 - \text{erf}\left(\sqrt{2}\frac{x - x_0}{w}\right)\right) \tag{A.1}$$

where P_0 is the power measured when detector completely covered (background), P_{max} is the maximum power on the detector, w is the beam waist, $x - x_0$ is the knife's displacement.

There are a few things overlooked in this analysis when comparing it to Figure 2-8, however. We assume a uniform area of the detector where any region will have an equal probability of absorption. This is clearly not our case since the PhCC has much higher detectability near the cavity than in other regions of the detector. This is why we do not see a clear error function, but a much sharper decline by moving away from cavity. Nonetheless, since we only need two points from the plot (it is standard practice to choose x and x' at the %10 and %90 power) and the beam waist is on the scale as the detector, this method can be used as a rough estimate.

The maximum power in our knife-edge measurement is when the beam is centered at the cavity (Figure 2-8 at $x = 0$) with a photocurrent of 1.14nA. The $x_{10\%}$ and $x_{90\%}$ are extracted based on this value and equation A.1 is used to find the $w = 3.2\mu m$.

Appendix B

Numerical Analysis

B.1 MEEP Code: Generate and Analyze PhCC

```
# Meep transmission and reflection through a cavity
# formed by a periodic sequence of holes in a dielectric waveguide,
# with a defect formed by removing a hole.

#Code used to analyze output
# python phcc.py | tee phcc.out
# h5topng -RZc dkbluered -C phcc-eps-000000000.h5 phcc-hz-*.h5
# h5topng -S 3 *.h5
# convert *.png *.gif
# h5topng *.h5
# grep tmfreqs *.out
# grep flux1: holey-wvg-cavity.out > flux.dat

from __future__ import division

import argparse
import meep as mp
import math
```

```
def main(args):
    resolution = 30 # pixels/um

    # Lattice Parameters
    eps = 13          # dielectric constant of waveguide
    a = 0.4           # lattice constant
    r = 0.33*a        # radius of holes

    # Defect Parameters
    shrk = 0.1*a      # Shrinking of defect cell
    shft = 1+0.2      # Defect Shift
    # shrk = 0.31*a     # Shrinking of defect cell
    # shft = 1      # Defect Shift
    r2 = r #r2 = 0.297*a     # Bi-atomic effect

    t = 0.22          # thickness of block
    pad = 0.64        # padding between last hole and PML edge
    dpml = 2        # PML thickness

    layers = 31  #has to be odd
    N = 15   #has to be odd

    # sx = 2*(dpml+N*a) # size of cell in x direction
    # sy = args.sy  # size of cell in y direction (perpendicular to wvg.)
    sx = 2*(dpml+19*a)


    # w = (layers+1)*a/2
    w = (sx-2*dpml)/2 # width of flux region
    sy = w*1.25+2*dpml # size of cell in y direction (perpendicular to wvg.)
```

```
# cell = mp.Vector3(sx, sy, t+2*pad+2*dpml)
cell = mp.Vector3(sx, sy, t+2*pad+2*dpml)

blk = mp.Block(size=mp.Vector3(mp.inf, mp.inf, mp.inf),
               center=mp.Vector3(0,0,0),
               material=mp.Medium(epsilon=1.5))

blk2 = mp.Block(size=mp.Vector3(mp.inf, w, t),
                center=mp.Vector3(0,0,0),
                material=mp.Medium(epsilon=eps))

geometry = [blk, blk2]


# for defect: shrink defect holes, shift defect holes, remove H=1 hole
for i in range(int(-(N-1)/2),int((N-1)/2+1)):
    for j in range(int(-(layers-1)/2), int((layers-1)/2+1)):
        if (abs(j), abs(i)) in ((2,0) ,(1,1) ):
            if i>0:
                geometry.append(mp.Cylinder(shrk,
                                            height=t,
                                            center=mp.Vector3((i-(j%2)/2)*a*shft*
                                                math.sqrt(3), j*shft*a*0.5),
                                            material=mp.Medium(epsilon=1.5)))
            else:
                geometry.append(mp.Cylinder(shrk,
                                            height=t,
                                            center=mp.Vector3((i+(j%2)/2)*a*shft*
                                                math.sqrt(3), j*shft*a*0.5),
                                            material=mp.Medium(epsilon=1.5)))
        elif i==0 and j==0:
```

```
        geometry.append(mp.Cylinder(r,
                                    height=t,
                                    center=mp.Vector3(0, 0),
                                    material=mp.Medium(epsilon=eps)))
    else:
        if i>0:
            if (abs(i),abs(j)) in ((1,3) ,(2,0) ,(4,3) ,(0,6) ,(2,6) ):
                geometry.append(mp.Cylinder(r2,
                                            height=t,
                                            center=mp.Vector3((i-(j%2)/2)*a*
                                                math.sqrt(3), j*a*0.5),
                                            material=mp.Medium(epsilon=1.5)))
            else:
                geometry.append(mp.Cylinder(r,
                                            height=t,
                                            center=mp.Vector3((i-(j%2)/2)*a*
                                                math.sqrt(3), j*a*0.5),
                                            material=mp.Medium(epsilon=1.5)))
        elif i==0 and j%2==0:
            if (abs(i),abs(j)) in ((1,3) ,(2,0) ,(4,3) ,(0,6) ,(2,6) ):
                geometry.append(mp.Cylinder(r2,
                                            height=t,
                                            center=mp.Vector3(i*a*math.sqrt(3)
                                                , j*a*0.5),
                                            material=mp.Medium(epsilon=1.5)))
            else:
                geometry.append(mp.Cylinder(r,
                                            height=t,
                                            center=mp.Vector3(i*a*math.sqrt(3)
                                                , j*a*0.5),
                                            material=mp.Medium(epsilon=1.5)))
        elif i<0:
```

```
                if (abs(i),abs(j)) in ((1,3) ,(2,0) ,(4,3) ,(0,6) ,(2,6) ):
                    geometry.append(mp.Cylinder(r2,
                                                height=t,
                                                center=mp.Vector3((i+(j%2)/2)*a*
                                                    math.sqrt(3), j*a*0.5),
                                                material=mp.Medium(epsilon=1.5)))
                else:
                    geometry.append(mp.Cylinder(r,
                                                height=t,
                                                center=mp.Vector3((i+(j%2)/2)*a*
                                                    math.sqrt(3), j*a*0.5),
                                                material=mp.Medium(epsilon=1.5)))

    fcen = args.fcen  # pulse center frequency
    df = args.df      # pulse frequency width
    nfreq = 1000      # number of frequencies at which to compute flux

    sim = mp.Simulation(cell_size=cell,
                        geometry=geometry,
                        sources=[],
                        boundary_layers=[mp.PML(dpml)],
                        resolution=resolution)

# Whether to do a Q or Flux measurments
    if args.resonant_modes:
        # Define Source
        sim.sources.append(mp.Source(mp.GaussianSource(fcen, fwidth=df),
                                     component=mp.Ey,
                                     center=mp.Vector3(0.001,0.002),
                                     size=mp.Vector3()))

        # sim.symmetries.append(mp.Mirror(mp.Y, phase=-1))
```

```
    # sim.symmetries.append(mp.Mirror(mp.X, phase=-1))
    # sim.symmetries.append(mp.Mirror(mp.Z))

    sim.run(mp.at_beginning(mp.output_epsilon),
            mp.after_sources(mp.Harminv(mp.Ey, mp.Vector3(), fcen, df)),
            until_after_sources=400)

    sim.run(mp.at_every(1/fcen/20, mp.output_efield_y), until=1/fcen)
else:
    # Define Source
    sim.sources.append(mp.Source(mp.GaussianSource(fcen, fwidth=df),
                                 component=mp.Ey,
                                 center=mp.Vector3(),
                                 size=mp.Vector3()))

    #Epsilon 2D View
    # sim.run(mp.at_beginning(mp.output_epsilon),until_after_sources=1) # just
        run the dielectric scheme

    # Symmetry Boundry Conditions
    sim.symmetries.append(mp.Mirror(mp.X, phase=1))
    sim.symmetries.append(mp.Mirror(mp.Y, phase=1))
    sim.symmetries.append(mp.Mirror(mp.Z, phase=1))

    # Flux Region
    # in-plane flux region
    freg = mp.FluxRegion(center=mp.Vector3(0,0,t/2+pad/2),
                         size=mp.Vector3(w,w))

    # out-of-plane flux region
    # freg = mp.FluxRegion(center=mp.Vector3(0, 0, 0.6),
    #                      size=mp.Vector3(w, w))
```

```
        # transmitted flux
        trans = sim.add_flux(fcen, df, nfreq, freg)

        vol = mp.Volume(mp.Vector3(), size=mp.Vector3(sx))

        sim.run(mp.at_beginning(mp.output_epsilon),
                mp.during_sources(mp.in_volume(vol, mp.to_appended("hz-slice", mp.
                    at_every(0.4, mp.output_hfield_z)))),
                until_after_sources=mp.stop_when_fields_decayed(50, mp.Ey, mp.
                    Vector3(0,0,t/2+pad/2), 1e-3))

        sim.display_fluxes(trans)  # print out the flux spectrum

if __name__ == '__main__':
    parser = argparse.ArgumentParser()
    parser.add_argument('-r', '--resonant_modes', action='store_true', default=False,
                        help="Compute resonant modes. Default is transmission
                            spectrum.")
    parser.add_argument('-N', type=int, default=15, help='number of holes on either
        side of defect')
    parser.add_argument('-sy', type=int, default=5, help='size of cell in y direction (
        perpendicular to wvg.)')
    parser.add_argument('-fcen', type=float, default=0.7, help='pulse center
        frequency')
    parser.add_argument('-df', type=float, default=0.3, help='pulse frequency width')
    args = parser.parse_args()
    main(args)
```